2014-01-1987
Published 04/01/2014

doi:10.4271/2014-01-1987
saematman.saejournals.org

Compressive Behavior of Representative Volume Element Specimens of Lithium-Ion Battery Cells under Different Constrained Conditions

Shin-Jang Sung, Wei-Jen Lai, Mohammed Yusuf Ali, and Jwo Pan
Univ. of Michigan

Saeed Barbat
Ford Motor Co.

ABSTRACT

The compressive behavior of lithium-iron phosphate battery cells is investigated by conducting in-plane constrained compression tests and out-of-plane compression tests of representative volume element (RVE) specimens. The results for cell RVE specimens under in-plane constrained compression tests without pre-strains and with pre-strains in the out-of-plane direction indicate that the load carrying capacity is characterized by the buckling of cell specimens. As the pre-strain increases, the nominal compressive stress-strain curve becomes higher. The nominal stress-strain curves in the out-of-plane direction were also obtained and used to determine the elastic moduli for the elastic buckling analyses of the cell components in the cell RVE specimens with different pre-strains. Based on the elastic buckling analyses for a beam with different lateral constraints due to different pre-strains in the out-of-plane direction, the number of half waves and the buckling stresses were obtained. The results indicate that the number of half waves and the buckling stress increase as the pre-strain increases. The general trends of the numbers of half waves and the buckling stresses are in agreement with those obtained from experiments.

CITATION: Sung, S., Lai, W., Ali, M., Pan, J. et al., "Compressive Behavior of Representative Volume Element Specimens of Lithium-Ion Battery Cells under Different Constrained Conditions," *SAE Int. J. Mater. Manf.* 7(2):2014, doi:10.4271/2014-01-1987.

INTRODUCTION

Lithium-ion batteries have been considered for electric vehicles for the automotive industry due to its lightweight and high energy density. For automotive applications, the mechanical performance is of great importance for crashworthiness analyses. Mechanical tests such as shock, drop, penetration, roll-over, and crush tests for abuse conditions of battery cells, modules and packs were documented in SAE J2462 [1]. Research works were conducted on the safety performance of the battery cells under mechanical tests such as nail penetration tests, round bar crush tests, and pinch tests, for example, see [2, 3, 4]. However, the research works on the mechanical behavior of the representative volume elements (RVEs) of lithium-ion batteries are quite limited. Sahraei et al. [5] conducted a series of mechanical tests and computational works on commercial $LiCoO_2$/graphite cells used for cell phones. The results indicate that the compressive mechanical behavior is characterized by the buckling and densification of the cell components. Other testing and modeling data available were also conducted on commercial $LiCoO_2$ cylindrical or prismatic battery cells [6,7]. However, this information is of limited use for researchers to model the mechanical performance of automotive high-voltage $LiFePO_4$ battery cells and modules for crashworthiness analyses.

Recently, Lai et al. [8,9] investigated the mechanical behaviors of lithium-iron phosphate battery cells and modules by conducting tensile tests of individual cell and module components, constrained compression tests of RVE specimens of dry cells and modules, and a punch test of a small-scale dry module specimen. For in-plane constrained compression tests of cell RVE specimens, the results indicate the load carrying behavior of cell RVE specimens is characterized by the buckling of cells with a wavelength approximately in the order of the thickness of the cells and the final densification of the cell components. They also tested module RVE specimens with different heights and the results indicate that the load carrying behavior of module RVE specimens is also characterized by the buckling of cells with a wavelength approximately in the order of the thickness of the cells and the final densification of the module components but relatively independent of the height of the tested specimens. For the cell RVE specimens, the initial elastic buckling mode of the cell RVE specimen under in-plane constrained compression can be correlated to the elastic buckling solution of a beam with lateral constraints. The development of the higher order buckling modes of the component sheets and the critical stresses observed in experiments are in agreement with the results of the analytical buckling solutions and the corresponding finite element analyses. The elastic buckling analyses also justify the length selection of the cell RVE specimens.

In this investigation, cell RVE specimens were first made from the individual cell components. In-plane constrained compression tests with different pre-strains in the out-of-plane direction were then conducted. Out-of-plane compression tests were also conducted. The nominal stress-strain curves, the numbers of half waves and the buckling stresses of the cell RVE specimens under in-plane constrained conditions with different pre-strains in the out-of-plane direction were also obtained from the experiments. Elastic buckling analyses of a beam with lateral constraints were then conducted. The numbers of half waves and the buckling stresses for the cell RVE specimens with different pre-strains from the elastic buckling analyses are then compared with the corresponding experimental results. Finally, some conclusions are made.

SPECIMENS

Figure 1(a) shows a schematic of a pouch cell and a cell RVE specimen with the X-Y-Z coordinate system. Here, X and Y are referred to as the in-plane directions and Z is referred to as the out-of-plane direction. A battery cell consists of five major components: cover sheet, anode, cathode, separator and electrolyte. Since the electrolyte is difficult to handle during assembly due to its toxicity, all the cell RVE specimens tested in this study were made without electrolyte at the University of Michigan. Table 1 lists all the detailed material and thickness information of the cell components. The cover sheet is composed of aluminum foil with polyamide and polypropylene layers on both sides bonded together by polyester-polyurethane and urethane-free adhesive, respectively. The thickness of the individual layers of the cover sheet are shown in Table 1 and the total thickness of the cover sheet is 0.111 mm. The anode and cathode selected for this study are graphite coated on copper foil and $LiFePO_4$ coated on aluminum foil, respectively. The copper foil has a thickness of 9 μm and the total thickness of the anode sheet is 0.2 mm. The aluminum foil has a thickness of 15 μm and the total thickness of the cathode sheet is 0.2 mm. Both the anode and cathode sheets are double-side coated. The separator is made of polyethylene with the porosity ranging from 36 to 44% and a thickness from 16 to 25 μm. All the cell components are purchased commercially.

A small cell RVE specimen with the dimensions is shown in Figure 1(b). Due to the slight thickness variation of each component sheet, four cell RVE specimens have the size of 25 mm × 25 mm × 5.0 mm and 25 mm × 25 mm × 4.7 mm. Figure 1(c) shows a side view of a portion of a cell RVE specimen with the individual cell components. The large red arrows shown in the figures indicate the in-plane compressive direction. As shown in Figure 1(c), the anode (shown in orange) and cathode (shown in gray) form alternating layers with two cover sheets (shown in light blue). The separators (shown in white) are located between electrodes and cover sheets. The cell RVE specimen is composed of 10 anode, 10 cathode, 21 separator and 2 cover sheets. The cell components were manually cut and assembled. No electrolyte was added for the dry cells. Due to the large specimen width in the X direction compared to the specimen thickness, the specimen width does not change before and after in-plane compression tests. Therefore, the specimens are subject to the plane strain conditions in the X direction under in-plane compression tests.

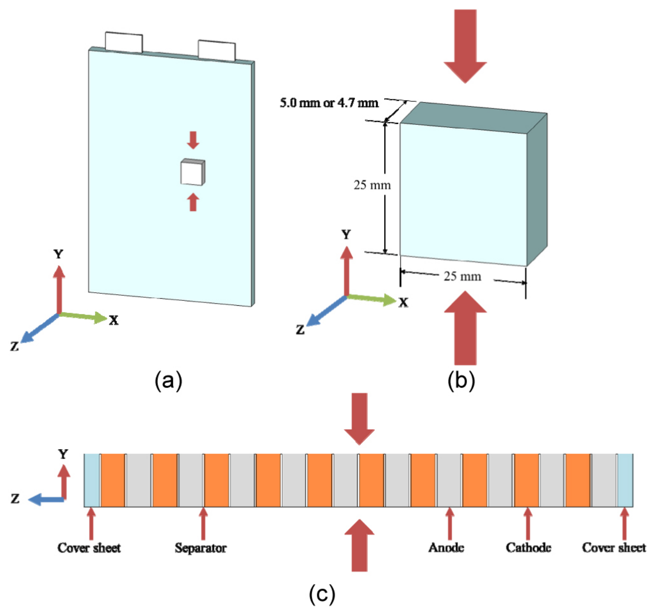

Figure 1. A schematic of (a) a pouch cell and a cell RVE specimen for the in-plane constrained compression test, (b) a cell RVE specimen with the dimensions, and (c) a side view of a small portion of the cell RVE specimen showing the individual cell components. The large red arrows indicate the compressive direction.

Figure 2(a) shows again a schematic of a pouch cell and a cell RVE specimen with the X-Y-Z coordinate system. A small out-of-plane compression cell RVE specimen is shown in Figure 2(b) with the dimensions. Figure 2(c) shows a side view of a small portion of the cell RVE specimen with the individual cell components. The large blue arrows shown in the figure indicate the out-of-plane compressive direction. The out-of-plane compression cell RVE specimen was smaller than the in-plane compression cell RVE specimen in order to avoid exceeding the load limit of the load cell. The size of the out-of-plane compression cell RVE specimen is reduced to 10 mm × 10 mm × 4.8 mm as shown in Figure 2(b). The layered structure of the cell RVE specimen is the same as that of the cell RVE specimen for in-plane constrained compression test.

Table 1. Specifications of cell components.

	Material	Thickness	
Cover sheet	Polyamide (JIS Z1714)	0.025 mm	0.111 mm
	Adhesive (Polyester-polyurethane)	4-5 g/m^2	
	Aluminum foil (JIS A8079, A8021)	0.040 mm	
	Adhesive (Urethane-free Adhesive)	2-3 g/m^2	
	Polypropylene	0.040 mm	
Anode sheet	Copper foil	9 μm	0.2 mm
	Graphite		
Cathode sheet	Aluminum foil	15 μm	0.2 mm
	$LiFePO_4$		
Separator sheet	Polyethylene (PE)	16-25 μm	

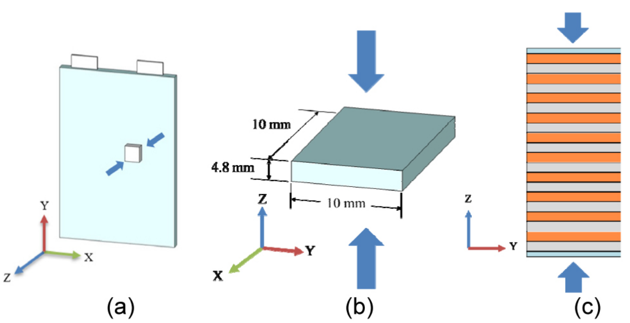

Figure 2. A schematic of (a) a pouch cell and a cell RVE specimen for the out-of-plane compression test, (b) a cell RVE specimen with the dimensions, and (c) a side view of a small portion of the cell RVE specimen showing the individual cell components. The large blue arrows indicate the compressive direction.

QUASI-STATIC COMPRESSION TESTS OF CELL RVE SPECIMENS

In-Plane Constrained Compression Tests of Cell RVE Specimens

Battery modules are usually held together by adhesive between the cells and the neighbor foam layers and aluminum heat dissipater sheets as well as two wrapping bands with tension. In the middle portion of a module, the cells are constrained by the neighbor foam layer and aluminum heat dissipater sheet. In an individual cell, the cell components can buckle individually with constraints from the neighbor cell components since there are no bonding forces between the cell components. Hence, a fully constrained die set was designed for constrained compression tests of cell RVE specimens. The punch and die setup for the in-plane constrained compression tests of cell RVE specimens is shown in Figure 3. The setup is composed of a male rectangular punch and a female die such that the specimen slot can be adjusted for different specimen geometries. A PMMA side window was made for recording the deformation process during the compression. The specimen slot in the die has an opening of 5 mm × 25 mm. Rectangular thin metal spacers with a thickness of 0.4 mm were made to adjust the width of the specimen slot such that different pre-strains of the specimens in the out-of-plane direction can be imposed. For the slot size of 4.6 mm × 25 mm and 4.2 mm × 25 mm, one and two spacers were inserted into the slot before tightening the two pieces of the die. For each of the specimen with a given pre-strain, a matching rectangular punch was made and used in the corresponding compression tests. These compression tests were conducted using a MTS Insight testing machine with a 10 kN load cell. The displacement rate is 0.5 mm/min (nominal strain rate of 0.0003 s^{-1}). The punch displacement was taken from the cross-head displacement recorded during the experiments.

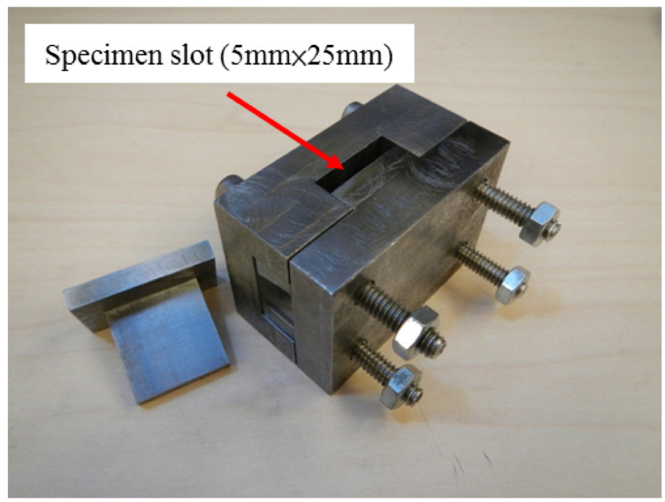

Figure 3. A punch and die setup for in-plane compression tests of cell RVE specimens.

Figure 4 shows the nominal compressive stress-strain curves of four cell RVE specimens tested at a displacement rate of 0.5 mm/min. The results in the figure show a nearly linear behavior in the beginning with the estimated effective compressive elastic moduli of 394 MPa, 665 MPa and 1032 MPa for the specimens with the out-of-plane pre-strains of 0.0%, 3.2% and 11.0%, respectively. As shown in Figure 4, for the results of the two specimens without the out-of-plane pre-strain, a noticeable change of slope takes place when the strain increases to about 1%. The change of the slope is due to the onset of the bucking of the cell components. Due to the buckling, the slope becomes smaller when the strain is larger than about 1%. As the strain continues to increase, the slope then gradually increases. Some minor stress drops were observed after the initial linear stage due to the development of kinks and shear bands.

For the specimen with the out-of-plane pre-strain of 3.2%, the estimated effective compressive modulus is larger than that of 0.0% in the initial linear stage. A noticeable change of slope takes place when the strain increases to about 1%. Again, due to the buckling, the slope becomes smaller when the strain is larger than about 1%. As the strain continues to increase, the slope then gradually increases. Also, some minor stress drops were observed after the initial linear stage due to the development of kinks and shear bands. For the specimen with the out-of-plane pre-strain of 11.0%, the estimated effective compressive modulus is the largest among the three pre strained cases in the initial linear stage. The slope change due to the onset of the bucking of the cell components is not prominent as those of the specimens with the out-of-plane pre-strains of 0% and 3.2%. As the strain continues to increase, the slope decreases slowly until the strain reaches about 14%. Then the slope starts to increase gradually as the strain increases. No stress drops were observed after the initial linear stage due to the severe constrained condition. As shown in Figure 4, the nominal stresses are higher for specimens with larger pre-strains. However, the general trends of the nominal stress-strain curves are quite consistent.

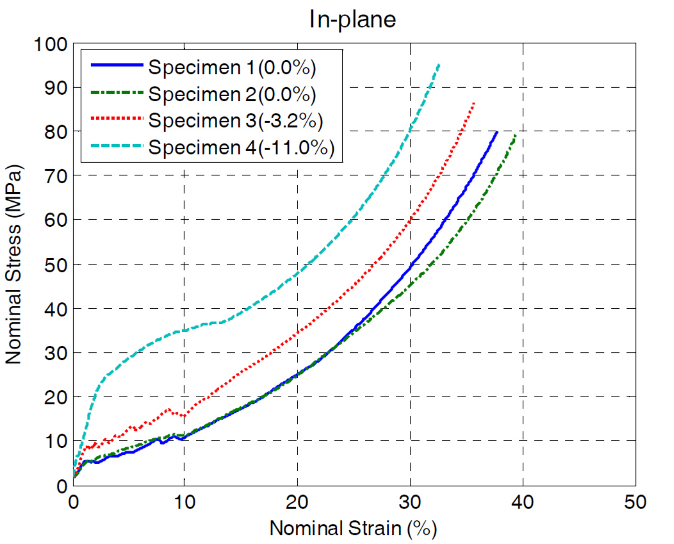

Figure 4. The in-plane nominal compressive stress-strain curves of four cell RVE specimens with the out-of-plane compressive pre-strains of 0%, 3.2% and 11%, tested at a displacement rate of 0.5 mm/min (nominal strain rate of 0.0003 s^{-1}).

Figures 5(a) and 5(b) show the front and back views of the tested cell RVE specimen without out-of-plane pre-strain. Figures 5(c) and 5(d) show the front and back views of the tested cell RVE specimen with the out-of-plane pre-strain of 3.2%. Figures 5(e) and 5(f) show the front and back views of the tested cell RVE specimen with the out-of-plane pre-strain of 11.0%. As shown in these figures, the kinks are fully developed to the folds and many irregular or incomplete shear band regions can be identified. After the efficient compaction mechanism of shear bands is completed, further compression can be accommodated by the micro buckling of the cell components outside the shear band regions and the compression in the shear band regions [8]. As shown in Figure 5, as the pre-strain increases, the number of the folds and kinks increases.

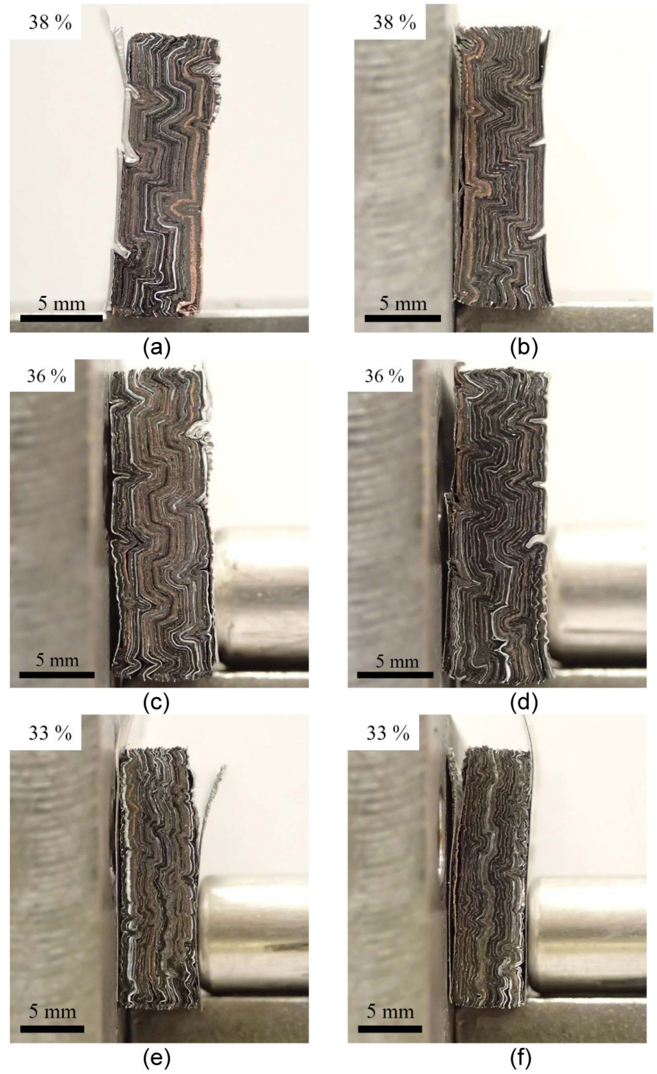

Figure 5. Deformation patterns of a cell RVE specimen after the in-plane constrained compression test at the displacement rate of 0.5 mm/min: (a) front and (b) back views of the RVE specimen with no out-of-plane pre-strain at the in-plane compressive strain of 38%; (c) front and (b) back views of the RVE specimen with the out-of-plane pre-strain of 3.2% at the in-plane compressive strain of 36%; (e) front and (f) back views of the RVE specimen with the out-of-plane pre-strain of 11.0% at the in-plane compressive strain of 33%.

Out-of-Plane Compression Tests of Cell RVE Specimens

The test was conducted using a MTS Insight testing machine with a displacement rate of 0.095 mm/min (nominal strain rate of 0.0003 s^{-1}). No constraint was applied to the lateral sides of the specimen in the X and Y directions. Two nominal compressive stress-strain curves of the cell RVE specimens under out-of-plane compression are shown in Figure 6. As shown in the figure, the low stress response in the early stage of the out-of-plane compression tests can be attributed to the consumption of the porosity in the cell components and the microscopic gaps between the cell components. With the increasing strain, densification of the cell components kicked in and contributed to the sharp increase of the stress. The nominal stress-strain curves appear to be linear elastic again at the strain of about 35% as the strain increases. This suggests that the total volume fraction of the porosity in the components and the microscopic gaps between the components is about 35% when the cell RVE specimens are nearly fully condensed and become linear elastic as the strain increases. The tested specimens retained the final thickness and appeared to be permanently deformed. However, no dimensional change before the strain of 50% was observed in the two lateral directions perpendicular to the loading direction, which implies that the Poisson's ratio can be assumed zero.

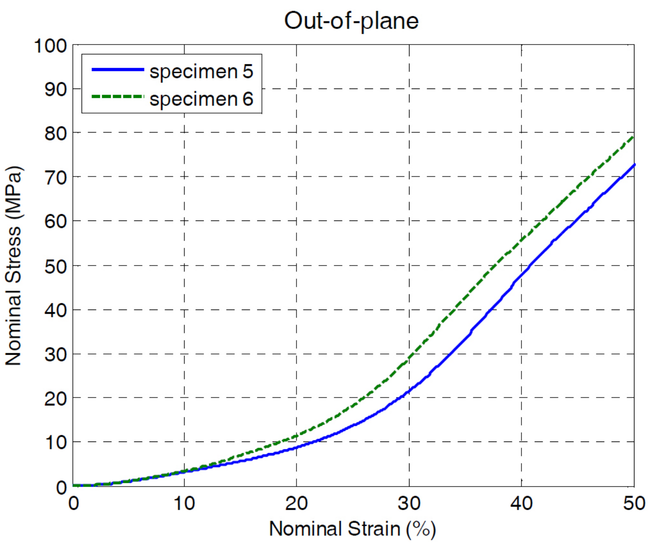

Figure 6. The out-of-plane nominal compressive stress-strain curves of cell RVE specimens tested at a displacement rate of 0.095 mm/min (nominal strain rate of 0.0003 s^{-1}).

Buckling Analyses of Cell RVE Specimens under In-Plane Constrained Compression

Based on the experimental observations of the cell RVE specimens under in-plane constrained compression, the physical mechanism to accommodate the compression begins with the elastic buckling of the cell components. When a cell RVE specimen was made, the component sheets were first assembled and packed together. The specimen was then put in the slot of the die. When a cell RVE specimen is under in-plane compression, the component sheets buckle independently with the lateral constraints from the neighbor component sheets. Since the component sheets were only packed together, each component sheet can be treated as an individual thin plate or beam under in-plane compression with the lateral constraints which can be treated as unattached elastic foundations.

Figure 7 shows a uniform straight beam under end loads and supported by two unattached elastic foundations. Both ends are hinged and the beam is supported by the elastic foundations through the lateral pressure p proportional to the deflection z in the Z direction. Here, k_1 and k_2 represent the spring constants of the harder and softer elastic foundations on the two sides of the beam, respectively. The buckling load solution of the beam can be found in [10, 11].

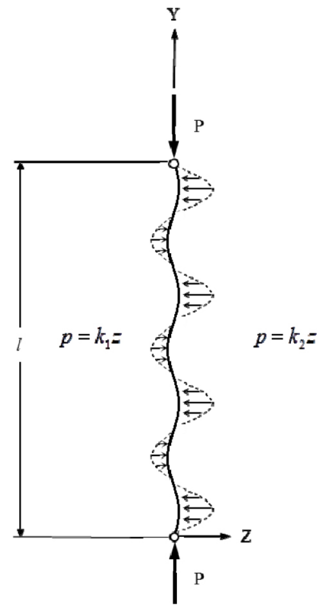

Figure 7. A schematic of a uniform straight beam under end loads and supported by unattached elastic foundations. Both ends are hinged and the beam is supported by the elastic foundations through the lateral pressure p proportional to the deflection z in the Z direction. The elastic foundations on two sides of the beam have the spring constants k_1 and k_2.

Table 2. Effective compressive elastic moduli of cell components (Lai et al. [8]).

	Effective Compressive Elastic Modulus. E_i' (MPa)
Cover sheet	575
Anode sheet	83
Cathode sheet	275
Separator sheet	90

For each anode, cathode, and separator sheet in the cell RVE specimen, the sheet can be considered as a beam with two unattached elastic foundations on both sides. For the anode, cathode and separator sheets in the middle portion of the cell RVE specimens, the buckling mode will be dominated by the constraints on both sides of the sheets. It is assumed that the spring constants for the elastic unattached foundations are the same and denoted by k for the cell components as beams in the middle portion of the cell RVE specimens. Here, k represents the lateral force per unit plate length per unit deflection of the neighbor components in the out-of-plane direction. The spring constant k can be expressed in terms of the out-of-plane compressive elastic modulus E of the cell RVE specimens as

$$k = \frac{Eb}{h} \tag{1}$$

where *h* represents the thickness of the neighbor cell components. With the elastic spring constant *k* on both sides of the beam is equal to each other, the buckling load of the *i* -th component with the two unattached elastic foundations is

$$P_m^i = \frac{m^2\pi^2 E_i' I_i}{L^2} + \frac{kL^2}{m^2\pi^2} \tag{2}$$

where *m* represents the number of half waves. Here, I_i $(= bh_i^3/12)$ is the moment of inertia for the *i* -th component. E_i' is the effective elastic modulus for a thin plate under plane strain compression conditions and is equal to $E_i/(1-\nu_i^2)$ where E_i and ν_i are the compressive elastic modulus and Poisson's ratio of the *i* -th component. The effective compressive elastic moduli for the cell components specimens without pre-strain are listed in Table 2 as in Lai et al. [8]. For the cell component specimens with pre-strains, the effective compressive elastic moduli are obtained by multiplying the ones for the component specimens without pre-strain by the ratio of the elastic compressive modulus from the in-plane compression tests of the cell RVE specimens with pre-strain to that without pre-strain, due to lack of experimental data. Here, *L*, *b* and h_i are the length, width, and thickness of the *i* -th component. Considering *m* as a real number as in Ali et al. [12], $\partial P_m^i/\partial m = 0$ gives

$$m = \left(\frac{k}{E_i' I_i}\right)^{\frac{1}{4}} \frac{L}{\pi} \tag{3}$$

The critical buckling load P_c^i can be determined as

$$P_c^i = 2(kE_i' I_i)^{\frac{1}{2}} \tag{4}$$

For a beam with one unattached elastic foundation on one side and a rigid wall on the other side, the elastic buckling solution is approximated by the elastic buckling solution for a beam with an unattached elastic foundation on one side and a rigid wall on the other side as discussed in Ali et al. [12]. For the cover sheets and the neighbor sheets, the buckling load of the *i* -th component can approximately be expressed as

$$P_n^i = \frac{4n^2\pi^2 E_i' I_i}{L^2} + \frac{3kL^2}{4n^2\pi^2} \tag{5}$$

where *n* represents the number of waves. Considering *n* as a real number as in Ali et al. [12], $\partial P_n^i/\partial n = 0$ gives

$$n = \left(\frac{3k}{16E_i' I_i}\right)^{\frac{1}{4}} \frac{L}{\pi} \tag{6}$$

The critical buckling load P_c^i can be determined as

$$P_c^i = 2\sqrt{3}(kE_i' I_i)^{\frac{1}{2}} \tag{7}$$

The values of the spring constant *k* can be estimated for the cover sheets and neighbor sheets near the die walls, and for the component sheets in the middle portion of the cell specimen. For the sheets in the middle portion of the cell specimen, the solution in Equations (3) and (4) can be used to estimate the buckling modes and loads of the component sheets as listed in Table 3. For the cover sheets and the neighbor sheets near the die walls, the buckling modes and loads can be estimated based on Equations (6) and (7) as listed in Table 3. Note that one wave of the cover sheets and the neighbor sheets near the die walls corresponds to two half waves of the component sheets in the middle portion of the cell RVE specimen.

The corresponding compressive strains at these buckling loads can be calculated by

$$\varepsilon_m^i = \frac{P_m^i}{E_i' A_i} \quad \text{or} \quad \varepsilon_n^i = \frac{P_n^i}{E_i' A_i} \tag{8}$$

for the component sheets in the middle portion or near the sides of the cell specimen. Here, A_i is the cross-sectional area of the *i* -th component. Equation (8) gives the strains at these buckling loads for the *i* -th components. The values are also listed in Table 3.

Table 3. Buckling modes, loads, and strains for the component sheets near the side and in the middle portion of the cell RVE specimens with different out-of-plane pre-strains and buckling stresses for the cell RVE specimens.

Pre-strain: 0.0%

	Side (k = 3.58 × 10^7 N/m^2)			
	Cover sheet	Anode	Cathode	Separator
n	11.3	11.9	8.8	64.8
P_n^i (N)	26.528	24.601	44.780	0.795
ε_n^i	0.0166	0.0593	0.0326	0.0177
Cell buckling stress σ_{cell} (MPa) at the component buckling strain ε_n^i	3.156	11.255	6.1830	3.356

	Middle (k = 7.29 × 10^7 N/m^2)		
	Anode	Cathode	Separator
m	21.4	15.9	117.1
P_m^i (N)	20.087	36.562	0.649
ε_m^i	0.0484	0.0266	0.0144
Cell buckling stress σ_{cell} (MPa) at the component buckling strain ε_m^i	9.189	5.048	2.740

Table 3. Buckling modes, loads, and strains for the component sheets near the side and in the middle portion of the cell RVE specimens with different out-of-plane pre-strains and buckling stresses for the cell RVE specimens.

Pre-strain: 3.2%

	Side (k = 1.55 × 10^8 N/m^2)			
	Cover sheet	Anode	Cathode	Separator
n	14.3	15.0	11.1	82.0
P_n^i (N)	71.718	66.510	121.063	2.150
ε_n^i	0.0266	0.0950	0.0522	0.0283
Cell buckling stress σ_{cell} (MPa) at the component buckling strain ε_n^i	8.533	30.427	16.716	9.072

	Middle (k = 3.17 × 10^8 N/m^2)		
	Anode	Cathode	Separator
m	27.2	20.1	148.2
P_m^i (N)	54.403	99.027	1.756
ε_m^i	0.0777	0.0427	0.0231
Cell buckling stress σ_{cell} (MPa) at the component buckling strain ε_m^i	24.889	13.673	7.408

Pre-strain: 11.0%

	Side (k = 3.76 × 10^8 N/m^2)			
	Cover sheet	Anode	Cathode	Separator
n	16.0	16.8	12.4	91.7
P_n^i (N)	139.210	129.100	234.992	4.174
ε_n^i	0.0333	0.1187	0.0652	0.0354
Cell buckling stress σ_{cell} (MPa) at the component buckling strain ε_n^i	16.564	59.061	32.447	17.609

	Middle (k = 7.72 × 10^8 N/m^2)		
	Anode	Cathode	Separator
m	30.4	22.5	165.7
P_m^i (N)	105.831	192.636	3.408
ε_m^i	0.0973	0.0535	0.0289
Cell buckling stress σ_{cell} (MPa) at the component buckling strain ε_m^i	48.416	26.599	14.378

The buckling loads of the cell RVE specimens when the cell components buckle can be obtained by summing over the loads of the cell components at the strains when the cell components buckle as

$$P_{cell} = \varepsilon_m^i \sum n_i E_i' A_i \quad \text{or} \quad P_{cell} = \varepsilon_n^i \sum n_i E_i' A_i \tag{9}$$

where n_i is the number of the i -th component in the cell RVE specimen according to the composite rule of mixture. The nominal buckling stress of the cell RVE specimen can be obtained by dividing the load by the cross-sectional area of the cell RVE specimen as

$$\sigma_{cell} = \frac{P_{cell}}{\sum A_i} \tag{10}$$

The buckling stresses for the cell RVE specimens are also listed in Table 3.

It should be noted that the results of the finite element analysis without pre-strain but with a small clearance between the cover sheets and the die walls in [12] suggest that the cover sheets actually buckle first. As listed in Table 3 for the cover sheets and the neighbor sheets, the cover sheets indeed buckle first for the cell RVE specimens with different pre-strains. The numbers of the half waves, the buckling stresses corresponding to the lowest buckling strains of the cover sheets, and the corresponding buckling strains are listed in Table 4. The experimental results are also listed in Table 4 for comparison. As listed in the Table 4, the general trends of the numbers of the half waves, the buckling stresses, and the corresponding buckling strains from the experiments are in agreement with those of the analytical results. It should be mentioned that the separators have slightly lower bucking strains and the corresponding buckling stresses for the cell RVE specimens with different pre-strains as listed in Table 3.

Table 4. A comparison between the experimental results and theoretical predictions of the numbers of half waves, the buckling stresses and the buckling strains for the specimens with the out-of-plane pre-strains of 0.0%, 3.2% and 11.0%.

Pre-strain	Experimental Results		
	n or $m/2$	Buckling stress σ_{cell} (MPa)	Buckling strain ε_{cell}
0.0%	4	4.7	0.01
3.2%	5	8.8	0.0117
11.0%	15	20.0	0.02

Pre-strain	Theoretical Predictions		
	n or $m/2$	Buckling stress σ_{cell} (MPa)	Buckling strain ε_{cell}
0.0%	11.3	3.156	0.0166
3.2%	14.3	8.563	0.0266
11.0%	16.0	16.564	0.0333

SUMMARY/CONCLUSIONS

The compressive behavior of lithium-iron phosphate battery cells is investigated by conducting in-plane constrained compression tests and out-of-plane compression tests of representative volume element (RVE) specimens. The results for cell RVE specimens under in-plane constrained compression tests without pre-strains and with pre-strains in the out-of-plane direction indicate that the load carrying capacity is characterized by the buckling of cell specimens. As the pre-strain increases, the nominal compressive stress-strain curve becomes higher. The nominal stress-strain curves in the out-of-plane direction were also obtained and used to determine the elastic moduli for the elastic buckling analyses of the cell components in the cell RVE specimens with different pre-strains. Based on the elastic buckling analyses for a beam with different lateral constraints due to different pre-strains in the out-of-plane direction, the number of half waves and the buckling stresses were obtained. The results indicate that the number of half waves and the buckling stress increase as the pre-strain increases. The general trends of the numbers of half waves and the buckling stresses are in agreement with those obtained from experiments.

REFERENCES

1. SAE International Surface Vehicle Recommended Practice, “Electric and Hybrid Electric Vehicle Rechargeable Energy Storage System (RESS) Safety and Abuse Testing,” SAE Standard J2464, Rev. Nov. 2009.
2. Nguyen, J. and Taylor, C., “Safety Performance for Phosphate Based Large Format Lithium-Ion Battery,” Telecommunications Energy Conference, INTELEC 2004. 26th Annual International: 146-148, 2004, doi:10.1109/INTLEC.2004.1401458.
3. Otsuki, M., Ogino, T., and Amine, K., “Investigation of Flame-Retardant Additives for Safety Usage of Lithium-Ion Batteries,” ECS Transactions 1(24):13-19, 2006, doi:10.1149/1.2209348.
4. Cai, W., Wang, H., Maleki, H., Howard, J., and Lara-Curzio, E., “Experimental Simulation of Internal Short Circuit in Li-Ion and Li-Ion-Polymer Cells,” Journal of Power Sources 196 (18):7779-7783, 2011, doi:10.1016/j.jpowsour.2011.04.024.
5. Sahraei, E., Hill, R., and Wierzbicki, T., “Calibration and Finite Element Simulation of Pouch Lithium-Ion Batteries for Mechanical Integrity,” Journal of Power Sources 201:307-321, 2012, doi:10.1016/j.jpowsour.2011.10.094.
6. Hill, R., “Development for a Representative Volume Element of Lithium-Ion Batteries for Thermo-Mechanical Integrity,” M.S. thesis, Mechanical Engineering Department, Massachusetts Institute of Technology, Cambridge, 2011.
7. Sahraei, E., Wierzbicki, T., Hill, R., and Luo, M., “Crash Safety of Lithium-Ion Batteries Towards Development of a Computational Model,” SAE Technical Paper 2010-01-1078, 2010, doi:10.4271/2010-01-1078.
8. Lai, W., Ali, M.Y., and Pan, J., “Mechanical Behavior of Representative Volume Elements of Lithium-ion Battery Cells under Compressive Loading Conditions,” Journal of Power Sources 245:609-623, 2014, doi:10.1016/j.jpowsour.2013.06.134.
9. Lai, W., Ali, M.Y., and Pan, J., “Mechanical Behavior of Representative Volume Elements of Lithium-Ion Battery Modules under Various Loading Conditions,” Journal of Power Sources 248:789-808, 2014, doi:10.1016/j.jpowsour.2013.09.128.
10. Young, W.C. and Budaynas, R.G., “Roark's Formulas for Stress and Strain,” 7th edition, McGraw-Hill, New York, ISBN 0-07-072542-X:714-725, 2001.
11. Timoshenko, S., “Theory of Elastic Stability,” 2nd edition, McGraw-Hill, New York, ISBN 0-07-Y85821-7:94-98, 1961.
12. Ali, M.Y., Lai, W., and Pan, J., “Computational Models for Simulations of Lithium-Ion Battery Cells under Constrained Compression Tests,” Journal of Power Sources 242:325-340, 2013, doi:10.1016/j.jpowsour.2013.05.022.

CONTACT INFORMATION

Professor Jwo Pan
Mechanical Engineering
The University of Michigan, Ann Arbor, MI 48109-2125
Telephone: 734-764-9404
Fax: 734-647-3170
jwo@umich.edu

ACKNOWLEDGMENTS

The support of this work by the Ford University Research Program is greatly appreciated. Helpful discussions with Dr. Tau Tyan of Ford Motor Company are greatly appreciated.